

High-Performance Bifunctional Metasurfaces in Transmission and Reflection Geometries

Tong Cai, ShiWei Tang, GuangMing Wang, HeXiu Xu, ShuLin Sun, Qiong He,*
and Lei Zhou*

Achieving multiple diversified functionalities in a single flat device is crucial for electromagnetic (EM) integration, but available efforts suffer the issues of device thickness, low efficiency, and restricted functionalities. Here, a general strategy to design high-efficiency bifunctional devices based on metasurfaces composed by anisotropic meta-atoms with polarization-dependent phase responses is described. Based on the derived general criterions, two bifunctional metadevices, working in reflection and transmission modes, respectively, that can realize two distinct functionalities with very high efficiencies ($\approx 90\%$ in reflection geometry and $\approx 72\%$ in transmission one) are designed and fabricated. Microwave experiments, including both far-field and near-field characterizations, are performed to demonstrate the predicted effects, which are in excellent agreement with numerical simulations. The findings in this study can motivate the realizations of high-performance bifunctional metadevices in other frequency domains and with different functionalities, which are of crucial importance in EM integration.

1. Introduction

Electromagnetic (EM) integration plays a central role in modern science and technology, since it is believed to be a key to solve the increasing demands on speed/memories of EM devices. A crucial scientific issue is that, how to *efficiently* integrate multiple *diversified* functionalities into one single device with *deep-subwavelength* size?

Multi-functional photonic devices (e.g., polarization beam splitters) have been realized by natural materials^[1] or recently proposed metamaterials (artificial manmade materials constructed by subwavelength microstructures with tailored photonic properties^[2,3]), but such systems are typically much thicker than wavelength, being inconvenient for photonic integration. Metasurfaces, planar inhomogeneous metamaterials composed of carefully selected

“meta-atoms” with specific EM responses, have attracted much attention recently due to their strong abilities to manipulate the wave-front of transmitted and reflected EM waves.^[4–45] By controlling the local phases on the wave-front of the beam incident on the metasurface,^[4] many fascinating phenomena were discovered, including the generalized law of refraction/reflection,^[4,5] perfect conversion between propagating wave (PW) and surface wave (SW),^[6,7] high-efficiency wave plates,^[8–10] meta-holograms,^[11] focusing,^[12–14] and other related effects.^[15–25] Very recently, considerable efforts were devoted to employing metasurfaces to design multi-functional optical devices.^[26–32] However, either the realized multi-functionalities are identical or similar (e.g., polarization-dependent hologram^[26–28] and focusing^[29]), or the involved meta-atoms exhibit complicated 3D non-flat structures,^[30] or the achieved working efficiencies are very low.^[31,32]

In this paper, we present a general strategy to design bifunctional metadevices to achieve *distinct* functionalities with very high efficiencies. As a proof of concept, we experimentally realize two bifunctional metadevices in the microwave regime based on flat meta-atoms, working in reflection and transmission geometries, respectively, which possess simultaneously the functionalities of focusing and beam bending (or even PW-SW conversion). We experimentally demonstrate that our devices can exhibit very high working efficiencies for two *distinct* functionalities, since the desired functionalities are linked with two polarization-related responses of the “meta-atoms” and thus can be tuned independently. This is in sharp contrast to the recently

T. Cai, Dr. H.X. Xu, Dr. Q. He, Prof. L. Zhou
State Key Laboratory of Surface Physics
Key Laboratory of Micro and Nano Photonic
Structures (Ministry of Education)
Department of Physics
Fudan University
Shanghai 200438, China
E-mail: qionghe@fudan.edu.cn; phzhou@fudan.edu.cn



T. Cai, Prof. G.M. Wang, Dr. H.X. Xu
Air and Missile Defend College
Air force Engineering University
Xi'an 710051, China

Dr. S.W. Tang
Department of Physics
Faculty of Science
Ningbo University
Ningbo 315211, China

Prof. S.L. Sun
Shanghai Engineering Research Center of Ultra-Precision
Optical Manufacturing
Green Photonics and Department of Optical
Science and Engineering
Fudan University
Shanghai 200433, China

Dr. Q. He, Prof. L. Zhou
Collaborative Innovation Center
of Advanced Microstructures
Nanjing 210093, China

DOI: 10.1002/adom.201600506

proposed geometric-phase-based multi-functional devices,^[31,32] which combine two sets of functional units naively and thus inevitably suffer the mutual interferences between two functionalities. Our findings pave the road to realize *high-efficiency flat* metadevices with *diversified* functionalities integrated, which may yield many applications in low-frequency photonics.

2. Concept

We now describe our strategy to design a multi-functional metadevice. Different from the geometric-phase systems adopted in refs. [15,28,31–33], where the local symmetric axes of meta-atoms are rotated as a function of position, here the system that we consider is composed by meta-atoms exhibiting global mirror symmetries with respect to $x \rightarrow -x$ and $y \rightarrow -y$ operations. Thus, the EM characteristics of the meta-atom located at a position $\vec{r} = (x, y)$ are described by two diagonal Jones' matrices: $\mathbf{R}(x, y) = \begin{pmatrix} r_{xx}(x, y) & 0 \\ 0 & r_{yy}(x, y) \end{pmatrix}$ and $\mathbf{T}(x, y) = \begin{pmatrix} t_{xx}(x, y) & 0 \\ 0 & t_{yy}(x, y) \end{pmatrix}$, where $r_{xx}, r_{yy}, t_{xx}, t_{yy}$ denote the reflection/transmission coefficients for that very meta-atom. To ensure high efficiencies for the designed metasurfaces, here we consider two ideal situations: (1) a totally reflective metasurface with $\mathbf{T} \equiv 0$ and $|r_{ii}(x, y)| = 1$, and (2) a totally transmissive one with $\mathbf{R} \equiv 0$ and $|t_{ii}(x, y)| = 1$. In both cases, however, the phases related to the scattering coefficients of the meta-atoms

can strongly depend on their local positions. These two phase distributions, denoted by $\varphi_{xx}(x, y)$ and $\varphi_{yy}(x, y)$, respectively, completely govern the scattering properties of the metasurface, and should be designed to follow certain conditions in order to realize the desired functionalities.

Let us discuss the simplest approach to realize a bifunctional device. Since an incident wave polarized along \hat{x} (or \hat{y}) direction can only "see" the phase distribution $\varphi_{xx}(x, y)$ (or $\varphi_{yy}(x, y)$), we can independently engineer $\varphi_{xx}(x, y)$ and $\varphi_{yy}(x, y)$ to realize two different functionalities, which can be triggered, respectively, by the incident waves polarized along x and y directions. For definiteness, here we present two bifunctional devices, working in reflection and transmission geometries, that can behave as focusing lenses and beam deflectors for incident waves with polarizations $\vec{E} \parallel \hat{y}$ and $\vec{E} \parallel \hat{x}$ (see Figure 1), respectively. To achieve this end, we require that $\varphi_{yy}(x, y)$ should satisfy the following parabolic distribution

$$\varphi_{yy}(x, y) = k_0 \left(\sqrt{F^2 + x^2 + y^2} - F \right) \quad (1)$$

where F is the focal length and $k_0 = \omega/c$ (see inset to Figure 1a,c), and that $\varphi_{xx}(x, y)$ must satisfy the following linear distribution (see inset to Figure 1b,d)

$$\varphi_{xx}(x, y) = C_1 + \xi \cdot x \quad (2)$$

with C_1 being a constant and ξ being the phase gradient provided by the metasurface that determines the bending angle

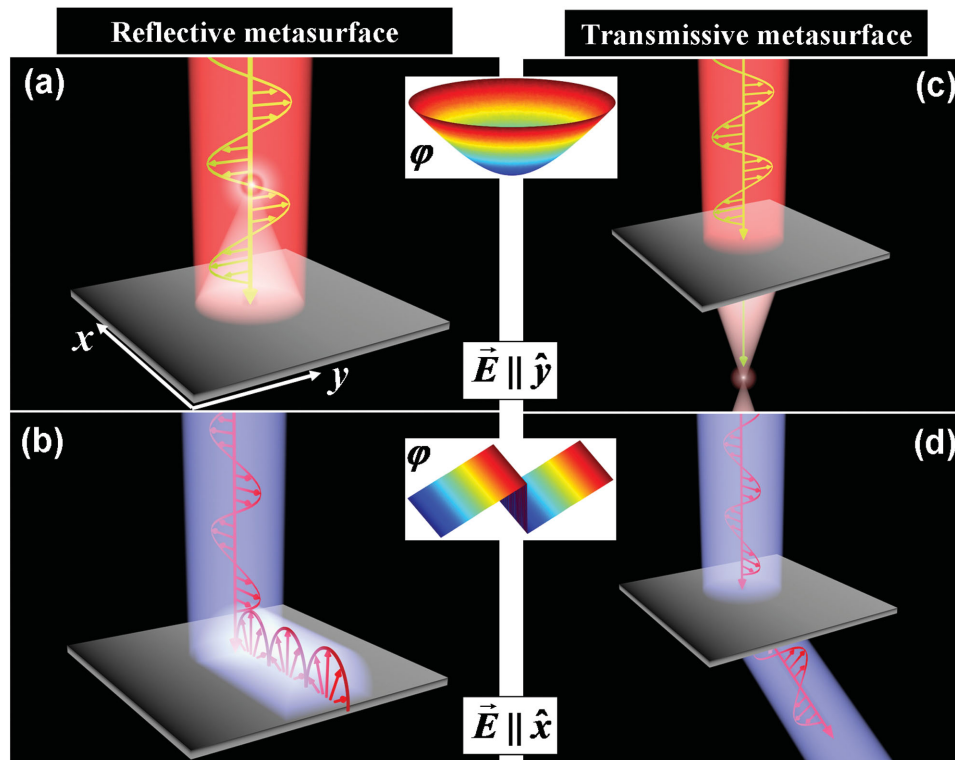


Figure 1. Schematics and working principles of the bifunctional metasurfaces. For reflection geometry, the metasurface behaves as a) a focusing lens and b) a PW-SW convertor when excited by incident waves with polarizations $\vec{E} \parallel \hat{y}$ and $\vec{E} \parallel \hat{x}$, respectively. For transmission geometry, the metasurface behaves as c) a focusing lens and d) a beam deflector when excited by incident waves with polarizations $\vec{E} \parallel \hat{y}$ and $\vec{E} \parallel \hat{x}$, respectively. Insets schematically depict the phase profiles of the metasurfaces in responses to excitations with different polarizations.

through the generalized Snell's law $k'_x = k_x^{\text{in}} + \xi$.^[4–6] Here, k_x^{in} is the parallel wave-vector of the incident beam and k'_x is the parallel wave-vector of the outgoing beam, which is the reflected or transmitted beam in different configuration. In particular, when the condition $\xi > k_0$ is satisfied, the metasurface can convert an incident PW to a SW.

Equations (1) and (2) are two criterions that guide us to design our bifunctional metadevices. We note that these criterions can be easily modified to meet other bi-functionality requirements. In the following two sections, to illustrate the basic ideas, we choose the microwave regime to design and characterize two high-efficiency bifunctional metasurfaces, working in reflection and transmission geometries, respectively.

3. Reflective Bifunctional Metasurface

We first design a reflective bifunctional metasurface. As shown in **Figure 2a**, the basic meta-atom is a sandwich structure, consisting of a metallic patch resonator with size $a \times b$ and a continuous metal sheet, separated by a 1.2 mm thick FR4 spacer. Such a structure, widely used in designing high-efficiency reflective metasurfaces at frequencies ranging from microwave to visible,^[34–36] is an ideal candidate for our purpose since the presence of a metallic ground plane naturally reflects all incoming wave back and thus we have $|r_{xx}| = |r_{yy}| = 1$

if we neglect material losses. Meanwhile, the reflection phase of such a structure undergoes a continuous -180° to 180° variation as frequency passes through a resonance at f_r which is dictated by the structural details (a, b, h , etc.) of the “meta-atom” (see inset to **Figure 2b**).^[34,38,39] As the result, at a fixed frequency $f_0 = 9.3$ GHz, we can tune these structural parameters (and thus the resonance frequency f_r) to get an arbitrary reflection phase as desired (see Section SA, Supporting Information, for the design strategy). In our numerical simulations, we have explicitly considered the dielectric losses by assuming the dielectric constant of the spacer layer as $\epsilon_r = 4 + 0.03i$, and assumed the metal as a perfect electric conductor since we are working in the microwave regime. **Figure 2b** depicts how the reflection phase φ_{yy} changes against varying the parameter a , with other geometric parameters fixed. Meanwhile, we note that φ_{yy} is insensitive to another parameter b , since the $\vec{E} \parallel \hat{y}$ resonance is predominantly determined by the length a , while b is responsible for the resonance associated with φ_{xx} . Such nearly independent control abilities on φ_{xx} and φ_{yy} offer us the possibilities to design the two-phase functions satisfying Equations (1) and (2), via carefully tuning a and b for “meta-atoms” located at different positions (see Section SA, Supporting Information, for more details).

We design such a metadvice with focal length $F = 90$ mm (see Equation (1)) and phase gradient $\xi = 1.09k_0$ (see Equation (2)). The designed metasurface consists of 20×20 meta-atoms and exhibits a total dimension of $120 \text{ mm} \times 120 \text{ mm}$ (see Section SA,

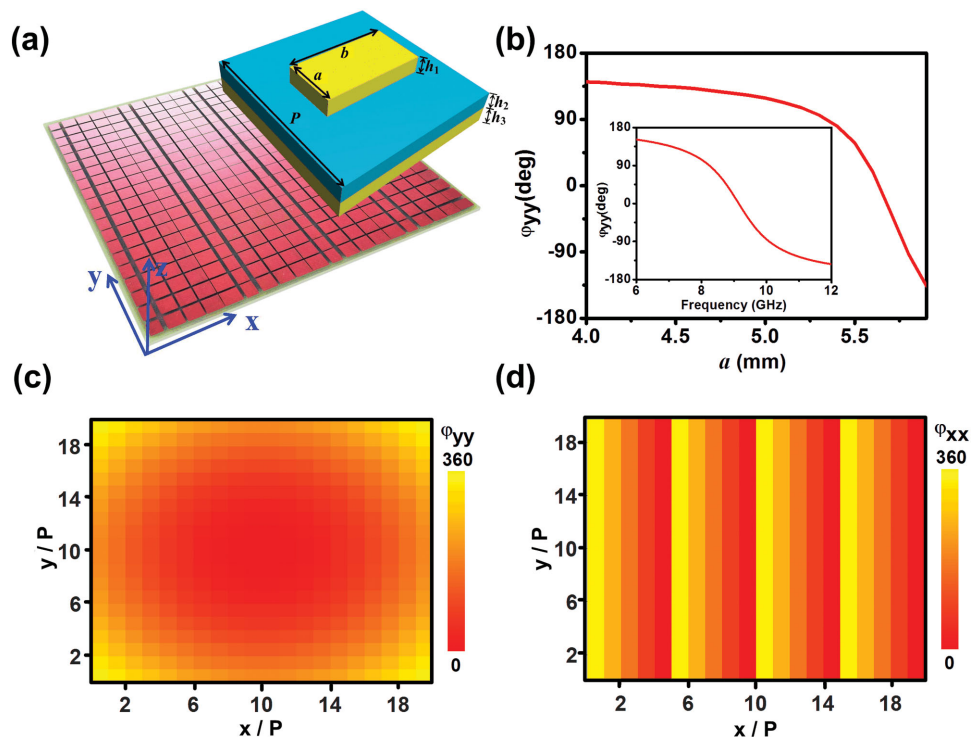


Figure 2. Design of the reflective bifunctional metasurface. a) Photograph of the fabricated sample. Inset shows the structure of a typical meta-atom consisting of a metal patch sized $a \times b$ and a continuous metal film separated by a FR4 spacer ($\epsilon_r = 4 + 0.03i$, $h_2 = 1.2$ mm). The meta-atom has a fixed size ($P = 6$ mm), and the thickness of the metal film is fixed as $h_1 = h_3 = 36$ μm . b) The FDTD computed reflection phase φ_{yy} for metasurfaces consisting of periodic array of meta-atoms with different parameters a and $b = 4$ mm fixed, at the frequency of $f_0 = 9.3$ GHz. Inset shows the FDTD computed reflection phase φ_{yy} as a function of frequency for a typical sample with $a = 5.6$ mm. c,d) FDTD simulated φ_{yy} and φ_{xx} distributions of designed/fabricated reflective metadvice at $f_0 = 9.3$ GHz.

Supporting Information, for its structural details), and the reflection phase distributions of each meta-atom for \hat{y} - and \hat{x} -polarized waves are shown in Figure 2c,d, respectively. Here the reflection amplitudes are nearly 1 for each meta-atom, due to the bottom metallic plate. We next fabricated the designed metadvice (see Figure 2a for its picture), and then characterized its bi-functionalities through microwave experiments.

We first examine the focusing property of our metadvice. Shining a \hat{y} -polarized microwave through a horn antenna normally onto the sample, we employed a monopole antenna to measure the electric-field distributions with an automatically controlled scanning mapper system.^[6,7] Both the monopole antenna and the horn are connected to a vector-field network analyzer (Agilent E8362C PNA), so that we can incorporate the phase information into the measured data to obtain the $\text{Re}[\vec{E}]$ distribution. Figure 3a displays the measured $\text{Re}[\vec{E}]$ distributions on both xoz and yoz planes, indicating clearly that the incoming plane wave has been converged to a point at $F = 94$ mm, which is identified from the maximum-intensity position on the z axis (see Section SB, Supporting Information). The measured \vec{E} -field distributions right on the focal plane at $z = 94$ mm (inset to Figure 3b) reinforced the excellent focusing effect displayed in Figure 3a. The measured focal length ($F = 94$ mm) matches well with the theoretical design ($F = 90$ mm) and finite-difference-time-domain (FDTD) simulation result ($F = 91$ mm). The slight difference between the measured and designed values

can be attributed to the finite-size effect of the metasurface, the imperfections of the incoming wave-front and the sample fabrication errors. To quantitatively evaluate the working bandwidth of our lens, we depicted in Figure 3b the measured and simulated maximum electric-field amplitude as a function of frequency. At the working frequency $f_0 = 9.3$ GHz, the electric field is indeed the largest implying that the focusing performance is the best. At frequencies deviating from the working one, the focusing performance gets deteriorated since the phase profile φ_y no longer strictly follows the desired distribution Equation (1). The working bandwidth of our device, defined by the full width at half maximum (FWHM) of electric intensity, is about 2.8 GHz (8.4–11.2 GHz). Within the working frequency bandwidth, the focal-spot size varies in the range of 31–37 mm while the focal length changes between 86 and 115 mm (see Section SC, Supporting Information, for details). More importantly, the working efficiency of our meta-lens, defined by the ratio between the powers carried by the focal spot and the incident beam,^[46] lies in the range of 90.8%–91.2%, estimated based on our experimental results at the working frequency (see Sections SD and SE, Supporting Information).

We next examine the other functionality (i.e., a PW-SW convertor) of our metadvice. As discussed in ref. [6], a gradient metasurface with phase gradient $\xi > k_0$ can convert a PW to a SW since the “reflected” wave possesses a parallel k_x vector larger than k_0 (see Equation (2)). However, the generated SW is

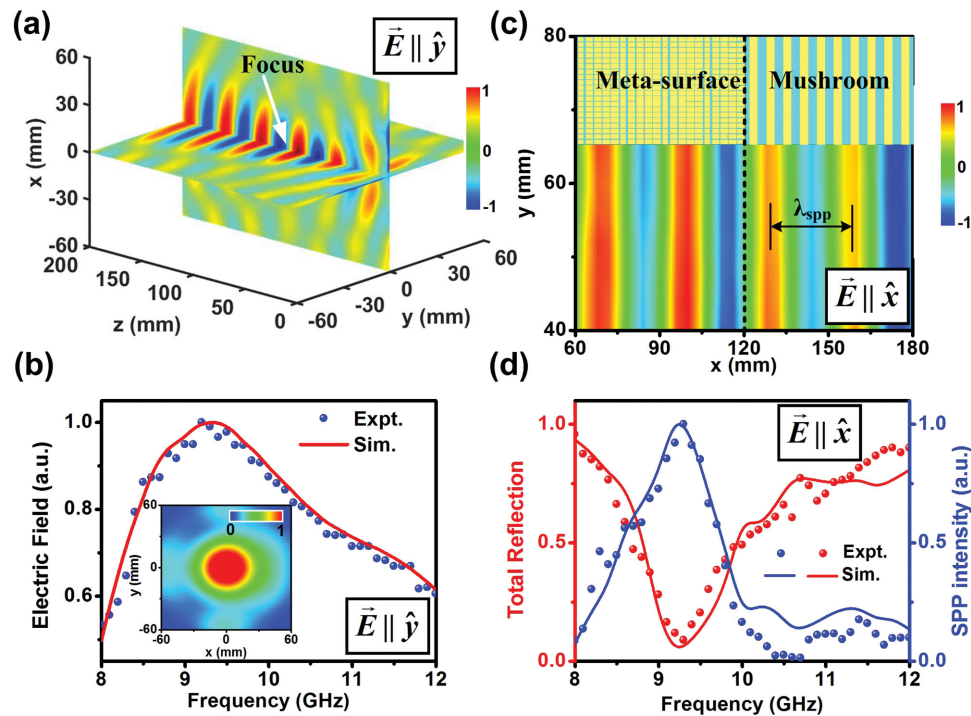


Figure 3. Characterizations of the reflective bifunctional metasurface. a) Measured $\text{Re}[\vec{E}]$ distributions on both xoz and yoz planes as the metasurface is illuminated by a normally incident \hat{y} -polarized plane wave at $f_0 = 9.3$ GHz. b) Measured and simulated \vec{E} -field amplitude spectrum at the focal point. The \vec{E} -fields are normalized against the maximum value in the spectrum. Inset depicts the measured $\text{Re}[\vec{E}]$ distribution on the xy plane with $z = 94$ mm. c) Measured $\text{Re}[\vec{E}]$ pattern on the xy -plane using a monopole antenna placed vertically and 8 mm above the metasurface and the mushroom structure, under the illumination of a normally incident \hat{x} -polarized plane wave at 9.3 GHz. d) Measured (points) and simulated (lines) spectra of the total reflection (red symbols, left axis) and the intensity of the SPP generated on the sample (blue symbols, right axis) under the illumination of an \hat{x} -polarized plane wave at a normal incident angle. The SPP intensities are the measured and simulated $|\vec{E}_z|^2$, which are normalized against their maximum value in the obtained spectrum, respectively.

not an eigenmode of the metasurface, but rather a driven SW which is only stable under the excitation of the PW. We follow refs. [6] and [40] to design and fabricate a mushroom structure supporting eigen spoof surface plasmon polariton (SPP) (see Section SF, Supporting Information, for more details) and put it at the right side of the metasurface to guide out the driven SW, as shown in the inset to Figure 3c. Illuminating the metasurface by an \hat{x} -polarized microwave at normal incidence, we measured both the total reflection (denoted by R) by the metasurface (R was obtained by integrating the scattered powers over all angle region) and the intensity of the spoof SPP generated on the mushroom converted from the driven SW on the metasurface. To ensure that only the metasurface part is illuminated by the incident wave, a 5 cm thick absorber layer was placed 20 mm above the mushroom surface to absorb any possible microwaves shining on the mushroom structure. The spectrum of the total reflection depicted in Figure 3d shows a pronounced dip at frequencies around $f_0 = 9.3$ GHz, implying that a large amount of the impinging energy has been transferred into the spoof SPP. To unambiguously demonstrate this point, we further adopted the near-field scanning technique to measure the local field distribution on both the metasurface and the mushroom structure right at the frequency of f_0 . The measured $\text{Re}[\vec{E}_z]$ pattern depicted in Figure 3c represents a very well-defined spoof SPP with a parallel wave-vector of $k_x = 206.5 \text{ m}^{-1}$, which is in good agreement with the theoretically calculated value ($k_{\text{SPP}} = 209.4 \text{ m}^{-1}$) at f_0 . At frequencies other than f_0 , the reflection to free space is enhanced while the conversion to SPP is decreased, which can be seen clearly in Figure 3d. The absolute PW-SW conversion efficiency is about 90% (simulation value: 92%), which is calculated by the equation $\eta = 1 - R$. Note that the working bandwidth of this functionality is about 1 GHz (8.7–9.7 GHz) estimated by the FWHM of the SPP intensity spectrum.

4. Transmissive Bifunctional Metasurface

We next design a high-efficiency bifunctional metasurface in transmission geometry. As discussed in Section 2, the first step is to find a collection of meta-atoms which are (nearly) totally transparent but with transmission phases (φ_{xx} and φ_{yy}) changeable via structural tuning. This is quite challenging since the variation in phase is typically linked with transmission amplitude in a transmissive system. Although transparent meta-atoms can be designed by 3D structures involving both electric and magnetic resonators, such meta-atoms are very complicated and non-flat in nature, being difficult to fabricate.^[30] To find appropriate transparent meta-atoms, we first note that a resonant unit containing a metallic mesh coupled with a metal patch (see inset to Figure 4a) can exhibit a perfect EM transmission at a particular frequency, induced by the interaction between the Lorentz resonator (i.e., the metal patch) and the opaque background (the metallic mesh).^[16,45] However, for a single particle, the transparency frequency window is quite narrow, and more importantly, the associated transmission phase only covers a very small range, which is a typical behavior of a single Lorentz resonator. This problem can be remedied by stacking more particles to form a

multilayer system. Utilizing the mutual interactions between these particles, both the transparency window and the transmission-phase variation range can be significantly enlarged, as shown in Figure 4b for a four-layer composite unit (see inset to Figure 4a). Figure 4b shows that within a wide transparency window (9.1–11.7 GHz), the variation of φ for such a meta-atom can cover a nearly 360° range while the transmission amplitude remains at a high value ($|t| > 0.8$) although it is not perfectly 100%. These interesting properties offer us the possibility to find a unit with an arbitrary transmission phase. We computed the transmission amplitude and phase as a function of a and b with FDTD simulations at $f_0 = 10.5$ GHz (see Section SA, Supporting Information). Based on these results, we tuned the lengths of the inner patch a and b to find a collection of high-transmission meta-atoms with transmission phases ($\varphi_{xx}, \varphi_{yy}$) satisfying Equations (1) and (2) in which $\xi = 0.43k_0$ and $F = 60$ mm. The designed transmission phase distributions φ_{yy} and φ_{xx} of each meta-atom are shown in Figure 4c,d, respectively, with corresponding transmission amplitudes $|t_{yy}|$ and $|t_{xx}|$ displayed in Figure 4e,f. The structural details of these meta-atoms can be found in Section SA (Supporting Information). We note that although the metallic mesh is not an absolutely necessary element in designing our meta-atoms, its presence can significantly reduce the mutual couplings between adjacent meta-atoms, which make our design robust and reliable.^[16] We then fabricated a sample with a total size of $132 \times 132 \text{ mm}^2$ (see Figure 4a for its picture) according to the design.

With the sample in hand, we now experimentally investigate its focusing functionality. The experimental configuration is quite similar to that of the reflection metadvice, except here the \vec{E} -field measurement is performed at the transmission side. Figure 5a shows the measured $\text{Re}[\vec{E}]$ distributions at both xoz and yoz planes, as the sample was shined by a \hat{y} -polarized wave at $f_0 = 10.5$ GHz. A focal point can be obviously seen at $F = 64$ mm, in good agreement with numerical simulation result ($F = 62$ mm) (see Section SB, Supporting Information). Here, the deviation from the theoretical value ($F = 60$ mm) is mainly due to the finite-size effect of our sample. The absolute working efficiency of the transmissive meta-lens, evaluated by the ratio between the powers carried by the focal spot and the incident one at $f_0 = 10.5$ GHz,^[46] lies in the range of 72.5%–73.6% based on experimental data (see Sections SD and SE, Supporting Information). As shown in Figure 5b, the working bandwidth of our lens is about 2.9 GHz (8.7–11.6 GHz), evaluated by the FWHM of intensity of \vec{E} -field. Within the bandwidth, the focal-spot size changes in the range of 17–20.5 mm while the focal length varies in the range of 43–70 mm (see Section SC, Supporting Information, for more details).

We finally characterized the beam-deflection functionality of our device. As schematically depicted in the inset to Figure 5c, illuminating our metadvice by a normally incident \hat{x} -polarized microwave, we measured the angular power distributions for both transmitted and reflected waves. Figure 5c shows clearly that, within a frequency interval from 10.2 to 11.3 GHz, most of the transmitted waves are deflected to an anomalous angle, described perfectly by the generalized Snell's law $\theta_t = \sin^{-1}(\xi/k_0)$ (solid stars in Figure 5c). Obviously, the best performance is found at the working frequency f_0

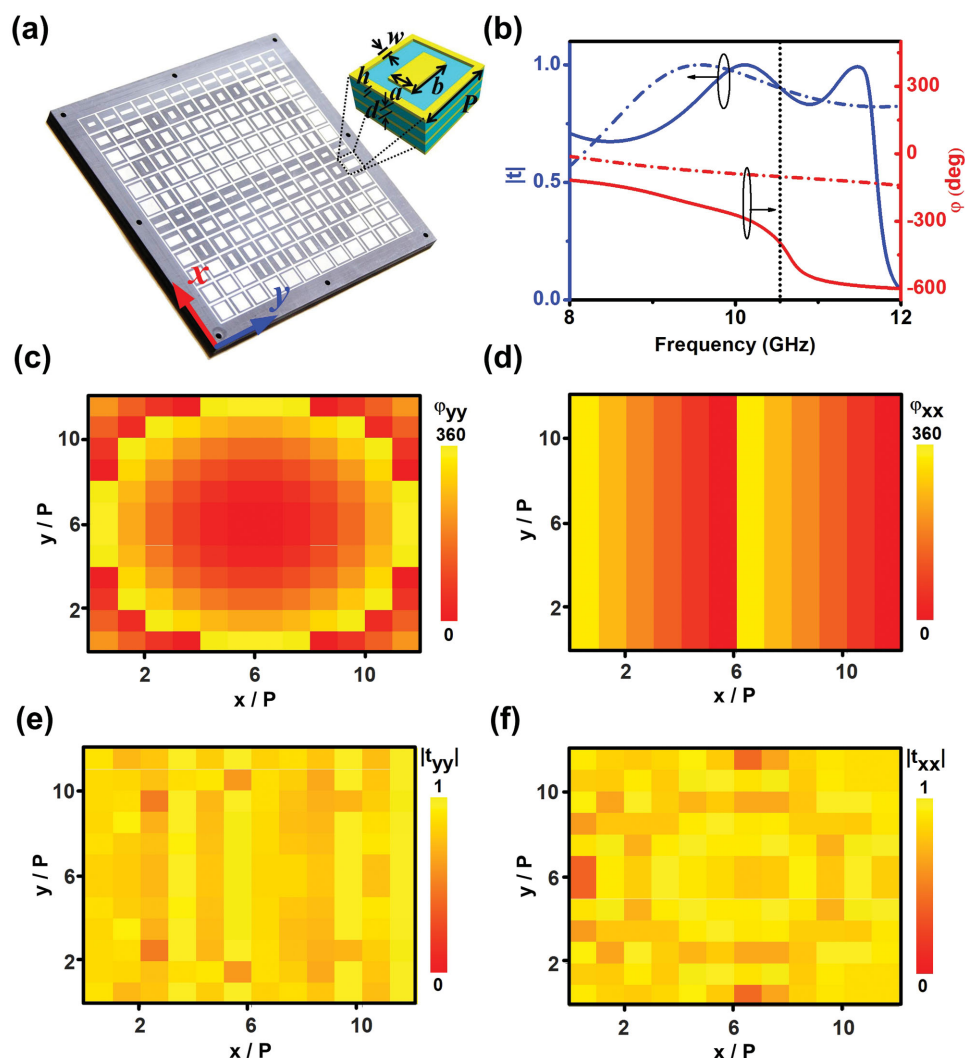


Figure 4. Design of the transmissive bifunctional metasurface. a) Photograph of the fabricated sample. Inset illustrates a typical meta-atom composed of four metallic layers separated by three F4B spacers ($\epsilon_r = 2.65 + 0.01i$, $d = 1.5$ mm). Other parameters are $P = 11$ mm, $w = 0.5$ mm, $h = 36$ μm . b) FDTD simulated spectra of transmission amplitude (blue lines) and phase (red lines) for the metasurface constructed by the periodic array of meta-atom with $a = 5$ mm and $b = 8.8$ mm, under the excitations of \hat{y} -polarized (solid lines) and \hat{x} -polarized (dotted lines) incident waves, respectively. c, d) FDTD simulated φ_{yy} and φ_{xx} distributions of the designed/fabricated transmissive metadvice at frequency $f_0 = 10.5$ GHz. e, f) FDTD simulated $|t_{yy}|$ and $|t_{xx}|$ distributions of the designed/fabricated transmissive metadvice at $f_0 = 10.5$ GHz.

(= 10.5 GHz), where the normal-mode transmission disappears nearly completely while the anomalous transmission reaches a maximum. Our experiment shows that the absolute efficiency of this functionality is 72% (simulation value: 73%), which is defined by the ratio between the power carried by the anomalously deflected beam and that of the incident beam, each obtained by integrating the power distribution over the angle regions related to the very beams. The missing power is mainly carried away by the reflected beam, since our meta-atoms are not ideally transparent (see Figure 4f). The achieved working efficiency (72%), although not reaching 100%, is already much higher than those for other available transmission metasurfaces,^[41–44] and can be further enhanced by optimizing our design (see Section SG, Supporting Information). Finally, we experimentally examined the $\theta_t \sim \theta_i$ relation for the anomalous refraction with frequency fixed at $f_0 = 10.5$ GHz,

where θ_t and θ_i denote the refraction and incident angles, respectively. As shown in Figure 5d, the measured results (blue star) are in perfect agreement with the FDTD simulations (solid red circle) and the analytical model based on the generalized Snell's law (green line).

5. Conclusions

In summary, we presented a general strategy to design high-efficiency metadvicees with distinct wave-manipulation functionalities integrated, and then fabricated two microwave bifunctional metadvicees, working in transmission and reflection geometries, respectively. Our near-field and far-field experiments show that the two devices, both with deep-subwavelength thicknesses, can exhibit focusing and wave bending (even

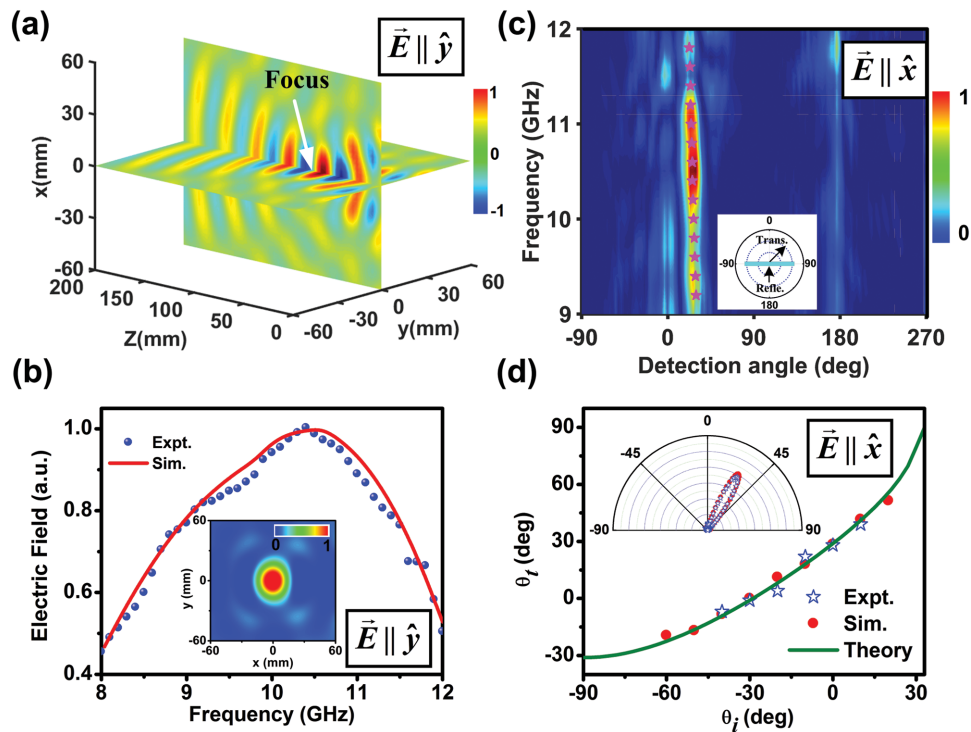


Figure 5. Characterizations of the transmissive bifunctional metasurface. a) Measured $\text{Re}[\vec{E}]$ distributions on both xoz and yoZ planes as the metasurface is illuminated by a normally incident \hat{y} -polarized plane wave at $f_0 = 10.5$ GHz. b) Measured and simulated \vec{E} -field amplitude spectra at the focal point. Inset depicts the measured $\text{Re}[\vec{E}]$ distribution at the xy plane with $z = 64$ mm at $f_0 = 10.5$ GHz. All \vec{E} -fields are normalized against the maximum value in the spectrum. c) Measured scattered wave intensity map as function of frequency and detection angle when the metasurface is illuminated by \hat{x} -polarized normally incident plane waves. d) Anomalous refraction angle θ_t versus the incident angle θ_i for our metasurface illuminated by an \hat{x} -polarized plane wave, obtained by experiments (blue open star symbols), FDTD simulations (red solid circle symbols), and theory (Generalized Snell's law,^[4] green lines) at $f_0 = 10.5$ GHz. Inset shows the measured and FDTD simulated angular distributions of the waves transmitted through the metasurface, illuminated by an \hat{x} -polarized wave at $f_0 = 10.5$ GHz.

PW-SW conversion) functionalities depending on the incident polarization, both of which are of very high efficiencies. Our results can stimulate the realizations of high-performance metadevices with other functionalities integrated, as well as in high-frequency regimes.

6. Experimental section

All samples were fabricated with a standard printed-circuit-board (PCB) technology. In our near-field experiments, the \vec{E} -field distributions presented in Figures 3 and 5 were measured by a home-made monopole antenna (≈ 30 mm long) which can be moved freely in 3D space controlled electrically. In the far-field experiments, we fixed the position of the source antenna, and then used another identical antenna as the receiver to measure the scattered-wave power. The receiver was placed 1.2 m away from the sample and can be freely moved on a circular track to collect the scattered signal in different directions. Detailed information on the experimental setup can be found in Section SH (Supporting Information).

Supporting Information

Supporting Information is available from the Wiley Online Library or from the author.

Acknowledgements

T.C. and S.W.T. contributed equally to this work. This work was supported by the National Natural Science Foundation China (Nos. 11474057, 11404063, 61372034, 61501499, 11674068, and 11604167), the MOE of China (B06011), the Shanghai Science and Technology Committee (Grant Nos. 14PJ1401200, 16ZR1445200, and 16JC1403100), and the Natural Science Foundation of Shaanxi province (Nos. 2016JM6063 and 2016JQ6001).

Received: June 30, 2016
Revised: September 16, 2016
Published online:

- [1] K. Shiraishi, T. Sato, S. Kawakami, *Appl. Phys. Lett.* **1991**, *58*, 211.
- [2] H. F. Ma, G. Z. Wang, W. X. Jiang, T. J. Cui, *Sci. Rep.* **2014**, *4*, 6337.
- [3] M. Moccia, G. Castaldi, S. Savo, Y. Sato, V. Galdi, *Phys. Rev. X* **2014**, *4*, 021025.
- [4] N. Yu, P. Genevet, M. A. Kats, F. Aieta, J. P. Tetienne, F. Capasso, Z. Gaburro, *Science* **2011**, *334*, 333.
- [5] X. Ni, N. K. Emani, A. V. Kildishev, A. Boltasseva, V. M. Shalae, *Science* **2012**, *335*, 333.
- [6] S. Sun, Q. He, S. Xiao, Q. Xu, X. Li, L. Zhou, *Nat. Mater.* **2012**, *11*, 426.
- [7] W. Sun, Q. He, S. Sun, L. Zhou, *Light: Sci. Appl.* **2016**, *5*, e16003.

- [8] S. Jiang, X. Xiong, Y. Hu, Y. Hu, G. Ma, R. Peng, C. Sun, M. Wang, *Phys. Rev. X* **2014**, *4*, 021026.
- [9] F. Ding, Z. Wang, S. He, V. M. Shalaev, A. V. Kildishev, *ACS Nano* **2015**, *9*, 4111.
- [10] Y. Yang, W. Wang, P. Moitra, I. I. Kravchenko, D. P. Briggs, J. Valentine, *Nano Lett.* **2014**, *14*, 1394.
- [11] L. Huang, X. Chen, H. Mühlenbernd, H. Zhang, S. Chen, B. Bai, Q. Tan, G. Jin, K. W. Cheah, C. W. Qiu, J. Li, T. Zentgraf, S. Zhang, *Nat. Commun.* **2013**, *4*, 2808.
- [12] M. Khorasaninejad, W. T. Chen, R. C. Devlin, J. Oh, A. Y. Zhu, F. Capasso, *Science* **2016**, *352*, 1190.
- [13] F. Aieta, M. A. Kats, P. Genevet, F. Capasso, *Science* **2015**, *347*, 1342.
- [14] A. Arbab, Y. Horie, A. J. Ball, M. Bagheri, A. Faraon, *Nat. Commun.* **2015**, *6*, 7069.
- [15] X. Chen, M. Chen, M. Q. Mehmood, D. Wen, F. Yue, C. W. Qiu, S. Zhang, *Adv. Opt. Mater.* **2015**, *3*, 1201.
- [16] T. Cai, G. M. Wang, F. X. Zhang, J. G. Liang, Y. Q. Zhuang, D. Liu, H. X. Xu, *IEEE Trans. Antennas Propag.* **2015**, *63*, 5629.
- [17] A. Pors, O. Albrektsen, I. P. Radko, S. I. Bozhevolnyi, *Sci. Rep.* **2013**, *3*, 2155.
- [18] H. F. Ma, G. Z. Wang, G. S. Kong, T. J. Cui, *Sci. Rep.* **2015**, *5*, 9605.
- [19] S. Liu, T. J. Cui, Q. Xu, D. Bao, L. Du, X. Wan, W. X. Tang, C. Ouyang, X. Y. Zhou, H. Yuan, H. F. Ma, W. X. Jiang, J. Han, W. Zhang, Q. Cheng, *Light: Sci. Appl.* **2016**, *5*, e16076.
- [20] X. Wan, T. Y. Chen, Q. Zhang, J. Y. Yin, Z. Tao, L. Zhang, X. Q. Chen, Y. B. Li, T. J. Cui, *Adv. Opt. Mater.* **2016**, DOI: 10.1002/adom.201600111.
- [21] S. L. Jia, X. Wan, D. Bao, Y. J. Zhao, T. J. Cui, *Laser Photonics Rev.* **2015**, *9*, 545.
- [22] C. Pfeiffer, C. Zhang, V. Ray, L. J. Guo, A. Grbic, *Phys. Rev. Lett.* **2014**, *113*, 023902.
- [23] C. Pfeiffer, A. Grbic, *Phys. Rev. Appl.* **2014**, *2*, 044011.
- [24] A. Y. Zhu, A. I. Kuznetsov, B. Luk'yanchuk, N. Engheta, P. Genevet, *Nanophotonics* **2016**, DOI: 10.1515/nanoph-2016-0032.
- [25] M. F. Farahani, H. Mosallaei, *Opt. Lett.* **2013**, *38*, 462.
- [26] Y. W. Huang, W. T. Chen, W. Y. Tsai, P. C. Wu, C. M. Wang, G. Sun, D. P. Tsai, *Nano Lett.* **2015**, *15*, 3122.
- [27] W. T. Chen, K. Y. Yang, C. M. Wang, Y. W. Huang, G. Sun, I. Chiang, C. Y. Liao, W. L. Hsu, H. T. Lin, S. Sun, L. Zhou, A. Q. Liu, D. P. Tsai, *Nano Lett.* **2014**, *14*, 225.
- [28] D. Wen, F. Yue, G. Li, G. Zheng, K. Chan, S. Chen, M. Chen, K. F. Li, P. W. H. Wong, K. W. Cheah, E. Y. B. Pun, S. Zhang, X. Chen, *Nat. Commun.* **2015**, *6*, 8241.
- [29] X. Wan, X. Shen, Y. Luo, T. J. Cui, *Laser Photonics Rev.* **2014**, *8*, 757.
- [30] C. Pfeiffer, A. Grbic, *Phys. Rev. Lett.* **2013**, *110*, 197401.
- [31] X. Ma, M. Pu, X. Li, C. Huang, Y. Wang, W. Pan, B. Zhao, J. Cui, C. Wang, Z. Y. Zhao, X. Luo, *Sci. Rep.* **2015**, *5*, 10365.
- [32] S. Chen, F. Yue, K. Chan, M. Chen, M. Ardron, K. F. Li, P. W. H. Wong, K. W. Cheah, E. Y. B. Pun, G. Li, S. Zhang, X. Chen, *Adv. Opt. Mater.* **2016**, *4*, 321.
- [33] W. Luo, S. Xiao, Q. He, L. Zhou, *Adv. Opt. Mater.* **2015**, *3*, 1102.
- [34] S. Ma, S. Xiao, L. Zhou, *Phys. Rev. B* **2016**, *93*, 045305.
- [35] G. Zheng, H. Mühlenbernd, M. Kenney, G. Li, T. Zentgraf, S. Zhang, *Nat. Nanotechnol.* **2015**, *10*, 308.
- [36] S. Sun, K. Yang, C. Wang, T. Juan, W. T. Chen, C. Y. Liao, Q. He, S. Xiao, W. Kung, G. Guo, L. Zhou, D. P. Tsai, *Nano Lett.* **2012**, *12*, 6223.
- [37] X. Li, S. Xiao, B. Cai, Q. He, T. J. Cui, L. Zhou, *Opt. Lett.* **2012**, *37*, 4940.
- [38] C. Qu, S. Ma, J. Hao, M. Qiu, X. Li, S. Xiao, Z. Miao, N. Dai, Q. He, S. Sun, L. Zhou, *Phys. Rev. Lett.* **2015**, *115*, 235503.
- [39] Z. Miao, Q. Wu, X. Li, Q. He, K. Ding, Z. An, Y. Zhang, L. Zhou, *Phys. Rev. X* **2015**, *5*, 041027.
- [40] M. J. Lockyear, A. P. Hibbins, J. R. Sambles, *Phys. Rev. Lett.* **2009**, *102*, 073901.
- [41] C. Pfeiffer, A. Grbic, *Appl. Phys. Lett.* **2013**, *102*, 231116.
- [42] J. Luo, H. Yu, M. Song, Z. Zhang, *Opt. Lett.* **2014**, *39*, 2229.
- [43] C. Pfeiffer, N. K. Emani, A. M. Shaltout, A. Boltasseva, V. M. Shalaev, A. Grbic, *Nano Lett.* **2014**, *14*, 2491.
- [44] Z. Wei, Y. Cao, X. Su, Z. Gong, Y. Long, H. Li, *Opt. Express* **2013**, *21*, 10739.
- [45] W. Sun, Q. He, J. Hao, L. Zhou, *Opt. Lett.* **2011**, *36*, 927.
- [46] P. Wang, N. Mohammad, R. Menon, *Sci. Rep.* **2016**, *6*, 21545.